Head and Neck Lesions: Characterization with Diffusion-weighted Echo-planar MR Imaging[1]

Jichen Wang, MD
Shodayu Takashima, PhD, MD
Fumiyoshi Takayama, MD
Satoshi Kawakami, MD
Akitoshi Saito, MD
Tsuyoshi Matsushita, MD
Mitsuhiro Momose, MD
Tetsuya Ishiyama, MD

Index terms:
Head and neck neoplasms, 20.343, 20.361, 20.362, 20.373, 20.379
Head and neck neoplasms, MR, 20.1214
Magnetic resonance (MR), diffusion study, 20.12144
Magnetic resonance (MR), echo planar, 20.121416

Published online: August 21, 2001
10.1148/radiol.2202010063
Radiology 2001; 220:621–630

Abbreviations:
ADC = apparent diffusion coefficient
CSF = cerebrospinal fluid
FOV = field of view
ROC = receiver operating characteristic
ROI = region of interest
SCC = squamous cell carcinoma

[1] From the Departments of Radiology (J.W., S.T., F.T., S.K., A.S., T.M., M.M.) and Otolaryngology (T.I.), Shinshu University School of Medicine, 3-1-1 Asahi, Matsumoto, Nagano 390-8621, Japan. From the 2000 RSNA scientific assembly. Received November 29, 2000; revision requested January 4, 2001; revision received February 28; accepted March 29. **Address correspondence to** S.T. (e-mail: *shodayu@hsp.md.shinshu-u.ac.jp*).

Author contributions:
Guarantor of integrity of entire study, S.T.; study concepts, J.W., S.T.; study design, J.W., F.T.; literature research, S.K., A.S.; clinical studies, T.I.; data acquisition, T.M., M.M.; data analysis/interpretation, F.T., S.K., A.S.; statistical analysis, J.W., S.T.; manuscript preparation, J.W., T.M., M.M.; manuscript definition of intellectual content, J.W., S.T.; manuscript editing, J.W.; manuscript revision/review, J.W., S.T.; manuscript final version approval, S.T., T.I.

PURPOSE: To evaluate whether apparent diffusion coefficients (ADCs) calculated from diffusion-weighted echo-planar magnetic resonance (MR) images can be used to characterize head and neck lesions.

MATERIALS AND METHODS: Diffusion-weighted echo-planar MR imaging was performed with a 1.5-T MR unit in 97 head and neck lesions in 97 patients. Images were obtained with a diffusion-weighted factor, factor *b*, of 0, 500, and 1,000 sec/mm^2, and an ADC map was constructed. The ADCs of lesions, cerebrospinal fluid, and spinal cord were calculated.

RESULTS: Acceptable images for ADC measurement were obtained in 81 (84%) patients. The mean ADC of malignant lymphomas, $(0.66 \pm 0.17[SD]) \times 10^{-3}$ mm^2/sec ($n = 13$), was significantly smaller ($P < .001$) than that of carcinomas. The mean ADC of carcinomas, $(1.13 \pm 0.43) \times 10^{-3}$ mm^2/sec ($n = 36$), was significantly smaller ($P = .002$) than that of benign solid tumors. The mean ADC of benign solid tumors, $(1.56 \pm 0.51) \times 10^{-3}$ mm^2/sec ($n = 22$), was significantly smaller ($P = .035$) than that of benign cystic lesions, $(2.05 \pm 0.62) \times 10^{-3}$ mm^2/sec ($n = 10$). No significant differences were seen in the mean ADC of cerebrospinal fluid and of spinal cord among four groups of lesions. When an ADC smaller than 1.22×10^{-3} mm^2/sec was used for predicting malignancy, the highest accuracy of 86%, with 84% sensitivity and 91% specificity, was obtained.

CONCLUSION: Measurement of ADCs may be used to characterize head and neck lesions.

Free diffusion is the process of random thermal motion of molecules, which is termed brownian motion, and this phenomenon can be measured and expressed as a diffusion coefficient. In biologic tissues, totally free diffusion of molecules does not exist due to restriction, such as that owing to cell membranes or molecular boundaries. In the human body, when diffusion is measured, it usually includes the component of the other kind of micromotion, which is called perfusion (1). Therefore, the extent of translational diffusion of molecules measured in the human body is referred to as the apparent diffusion coefficient (ADC). ADCs are expected to vary according to the microstructures of tissues or pathophysiologic states that are intrinsic to different tissues, and they can be obtained by calculating and measuring signal intensity in a series of diffusion-weighted MR images.

Tissue contrast attained by using diffusion-weighted magnetic resonance (MR) imaging is different from that attained by using conventional MR techniques. The diffusion technique involves the diffusion motion of water protons in the tissues, and this technique produces different contrast in different kinds of tissue. Therefore, the findings of this procedure can provide different information about diseased tissues. Diffusion-weighted MR imaging has been successfully used in the central nervous system for diagnosis of early cerebral ischemia (2–4), white matter disorders (5,6), and other brain diseases (7–9). Promising results have also been achieved by using this

technique in regions outside the central nervous system for differentiation between benign and malignant lesions in the liver (10,11) and bone marrow (12) and for identification of different cystic lesions in abdominal organs (13,14).

However, to our knowledge, there have been no articles about diffusion-weighted MR imaging applied to head and neck lesions, because the images in this area are likely to have susceptibility artifacts. Nonetheless, following the improvement of the echo-planar technique, some researchers (11,13) have demonstrated that diffusion-weighted echo-planar MR imaging can be successfully performed even in areas with high susceptibility artifacts. The purpose of our study was to evaluate whether ADCs calculated from diffusion-weighted echo-planar MR images can be used to characterize head and neck lesions.

MATERIALS AND METHODS

Subjects

Between October 1999 and July 2000, 97 consecutive patients (44 male patients, 53 female patients; mean age, 53 years; age range, 3–85 years) with head and neck lesions underwent diffusion-weighted echo-planar MR imaging after they provided informed consent. The study was approved by our institutional ethics committee. All patients had lesions larger than 1 cm in the greatest minimal transverse diameter on MR images and had not undergone biopsy or treatment with radiation therapy or chemotherapy before MR imaging. When the patients had multiple lesions with the same histologic diagnosis, only the largest one was used for calculation of ADCs. Among the 97 patients, eight patients had two lesions of different histopathologic characteristics, and the ADCs of the lesion that was the cause of the patient's chief complaint were calculated. Thus, this study consisted of 97 lesions, one in each patient. Of the 97 lesions, 23 lesions were located in the visceral space, 21 in the parotid space, 11 in the submandibular space, 13 in the oral cavity, 12 in the paranasal sinus and nasal cavity, nine in the carotid space, three in the pharyngeal mucosal space, two in the retropharyngeal space, and two in the posterior cervical space.

In 90 of the 97 lesions, the final diagnoses were made histologically by using either surgery (n = 73) or biopsy (n = 17). The diagnoses in three inflammatory lesions and one reactive lymph node were established with radiologic follow-up studies that revealed disappearance or remarkable regression of the lesions after initiation of antibacterial therapy. The diagnoses of three hemangiomas were based on typical radiologic findings, including those from dynamic computed tomography, MR imaging, and angiography (15).

MR Imaging Techniques

All MR examinations were performed with a 1.5-T whole-body MR unit (Symphony; Siemens Medical Systems, Erlangen, Germany) with head and/or neck circular polarization array surface coils. Before diffusion-weighted MR imaging, T1-weighted images (800/15 [repetition time msec/echo time msec], with two signals acquired) and T2-weighted fast spin-echo images (3,000/75, with two signals acquired) were obtained in the transverse plane, with a section thickness of 5 mm, an intersection gap of 1 or 2 mm, a field of view (FOV) of 19 × 22 cm, and an acquisition matrix of 224 × 256. A total of 18 transverse images covering the lesions and areas of drainage from regional lymph nodes were obtained. When necessary, one or more pulses of T1- or T2-weighted sequences were added in the coronal or sagittal plane, with the same pulse sequence parameters but with an FOV of 22 × 22 cm and an acquisition matrix of 240 × 256.

Subsequently, diffusion-weighted MR images were obtained at the section level where the largest transverse section of the lesion was identified on the MR images obtained before administration of contrast material. We avoided obvious cystic portions and calcified areas to perform diffusion-weighted MR imaging. Diffusion-weighted MR imaging was performed by using the multiple-section spin-echo single-shot echo-planar sequence in the transverse plane. In this sequence, diffusion weighting was achieved by applying a pair of motion-probing gradients, one before and the other after the 180° radio-frequency pulse of the spin-echo T2-weighted sequence. The motion-probing gradients were placed on all the directions of three gradients with the same strength. Diffusion sensitivity was determined with the motion-probing gradient factor b, where $b = \gamma^2 G^2 \delta^2 (\Delta - \delta/3)$. In this sequence, γ is the gyromagnetic ratio, and G, δ, and Δ are the gradient amplitude, gradient duration, and interval between diffusion gradient pulses, respectively.

Diffusion-weighted MR images were obtained at b factors of 0, 500, and 1,000 sec/mm^2 for each section in the same sequence. Three or five diffusion-weighted MR images were obtained during 42 seconds with the parameters of an echo time of 105 msec, a bandwidth of 1,116 Hz/pixel, an FOV of 30 cm, an acquisition matrix of 128 × 128, a section thickness of 3 mm, and an intersection gap of 1 or 2 mm. Then, ADC maps were automatically constructed for all diffusion-weighted MR images (b factors of 0, 500, and 1,000 sec/mm^2) by means of pixel-by-pixel calculation (16). Thus, four different trace images (diffusion-weighted MR images with b factors of 0, 500, 1,000 sec/mm^2 and an ADC map) for each section, with a pixel size of 2.3 × 2.3 mm, were obtained. We used the automatic multiangle-projection shim and fat-suppression technique to reduce the artifacts in diffusion-weighted MR images and applied an integrated phase correction during diffusion-weighted MR imaging. We also placed a special antisusceptibility device (Sat Pad; Alliance Pharmaceutical, San Diego, Calif) on the neck of all the patients to reduce susceptibility artifacts.

Next, we obtained T1-weighted images (680–800/15, with two signals acquired) in the transverse and coronal or sagittal planes immediately after an intravenous bolus injection of 0.2 mmol per kilogram of body weight of gadopentetate dimeglumine (Magnevist; Schering, Berlin, Germany) in all the patients.

Image and Pathologic Analyses

During the MR studies, two experienced radiologists (S.T., F.T.) evaluated the quality of diffusion-weighted MR images and determined by consensus whether they were acceptable for further analyses. They paid special attention to the image distortion caused by susceptibility artifacts and to the severity of chemical shift artifacts and ghosts in the phase-encoding direction. Then, one radiologist (J.W.) measured the signal intensity of the lesion with an electronic cursor to define the region of interest (ROI) in each patient. In measuring the signal intensity, ROIs were placed on the solid-appearing portions for the solid masses and on the cystic areas for the cystic lesions. The same radiologist also measured the signal intensity of the cerebrospinal fluid (CSF) and spinal cord in the upper area of the neck on diffusion-weighted MR images to assess the validity of our method and to compare our findings with the results in previous investigations. The signal

intensity for each lesion and each structure was measured three times and the value for each ROI that was 25 mm^2 or greater was included in the computation; an average value was used for analyses. The areas of ROIs were 112 $mm^2 \pm 29$ (SD) for the lesions, 34 $mm^2 \pm 5$ for the CSF, and 33 $mm^2 \pm 4$ for the spinal cord.

ADCs were calculated by using the following equation (17): $ADC = \ln[S_1/S_2]/b_2 - b_1$, where S_1 and S_2 are the signal intensities measured on diffusion-weighted MR images obtained with a lower *b* factor (b_1) and a higher *b* factor (b_2). Because the calculation of ADCs with this formula became more reliable as a difference between b_1 and b_2 became larger, we selected *b* factors of 0 and 1,000 sec/mm^2 for calculation of ADCs in this study.

We classified the lesions into four categories: malignant lymphomas, carcinomas (squamous cell carcinoma [SCC] or adenocarcinoma), benign solid tumors, and benign cystic lesions. We established a cystic lesion as an independent entity in this study, because this lesion had no solid portion for measurement of ADCs. The classification of solid lesions was based on the final diagnoses. We used a working formulation for clinical usage (18) for grading non-Hodgkin lymphomas.

In addition to cytologic and architectural features of tissues (19), ADC values are greatly affected by necrosis of tissues, especially liquefactive necrosis (20). We pathologically analyzed the amount of small foci of liquefactive necrosis in the tumors with SCC to know the correlation between the degree of small necrosis and the ADC values, because the tumors are likely to develop necrosis within themselves (21,22).

Without knowledge of the ADC values, one pathologist reviewed pathologic slides of solid-appearing tumors for the presence and the amount of small foci of liquefactive necrosis. Since tumor necrosis larger than 3 mm is reliably identified with MR imaging (22) and can be avoided for ADC measurement, we defined small foci of liquefactive necrosis as necrotic areas equal to or smaller than 3 mm in maximum diameter in pathologic specimens.

To quantitatively assess the degree of small necrotic foci in pathologic specimens, three FOVs in microscopy with fourfold magnification were randomly selected for examination of each tumor by the pathologist. Each FOV was photographed on 14 × 20-cm paper. We made a transparent overlay on which vertical and horizontal lines at an interval of 1 cm were drawn and put it on each photograph. The pathologist put the transparent overlay on each pathologic figure and counted the crossing points that corresponded to the necrotic foci on the photographs. He used the number as necrotic areas, and he also counted the crossing points that corresponded to the entire tumor and used the number as tumor areas. Then, a ratio of the number of necrotic areas to the number of tumor areas was calculated for each photograph, and an averaged value of three counts was used for assessment for each tumor. We graded the degree of small necrotic foci as mild and conspicuous types; the mild type indicated that the ratio of small necrosis was less than 0.20, and the conspicuous type indicated that the ratio was 0.20 or greater. Sufficient specimens for analysis were available in 18 solid-appearing SCCs.

Then, a mean ADC of the lesions in each category was calculated, and these mean ADCs were compared with each other. The mean ADCs of the CSF and the spinal cord in each group were also compared. The Kruskal-Wallis test was used for calculating the overall statistical differences, and the Mann-Whitney *U* test was conducted for calculating the differences in the mean ADCs between each pair in the four categories.

We used the receiver operating characteristic (ROC) curve to evaluate the diagnostic capability of the ADC value for use in the differentiation between malignant and benign lesions and in the differentiation between lymphoma and carcinoma. The ROC curves were calculated by using continuous data with a maximum likelihood method. We determined a threshold of ADC values, with which the highest accuracy was obtained for discriminating malignant from benign lesion and for discriminating lymphoma from carcinoma. The Mann-Whitney *U* test was used to calculate the difference in the mean ADCs between SCCs with the mild type and SCCs with the conspicuous type of small liquefactive necrosis. However, no correction factor was applied for the multiple testing; therefore, a *P* value less than .05 was considered to indicate a statistically significant difference. We used software (SPSS; SPSS, Chicago, Ill) for all statistical analyses. Finally, we proposed optimal ADC values for discrimination between benign and malignant lesions and for distinction between malignant lymphomas and carcinomas.

RESULTS

Among 97 patients, 16 (16%) had a local distortion that affected the lesions on diffusion-weighted MR images obtained with a *b* factor of 1,000 sec/mm^2, and their ADC maps were suboptimal due to susceptibility artifacts. Since the distortion artifacts may have caused inaccuracy in the signal intensity measurement, we excluded those 16 patients from this series. These lesions consisted of five (42%) of 12 lesions in the paranasal sinuses, six (26%) of 23 lesions in the areas near the larynx, three (23%) of 13 lesions in the oral cavity, and two (17%) of 12 lesions in the submandibular area. In addition, on diffusion-weighted MR images obtained with a *b* factor of 1,000 sec/mm^2, slight local susceptibility artifacts, chemical shift artifacts, and ghosts in the phase-encoding direction were observed in 35 (36%), 21 (22%), and 10 (10%) of 97 patients, respectively. However, these artifacts did not involve or overlap with the lesions and, therefore, did not preclude calculation of the ADCs of the lesions.

Thus, 81 lesions, one in each patient, qualified for ADC measurement, and their diagnoses are listed in Table 1. ADCs of the spinal cord were successfully measured in all 81 patients. However, we abandoned measurement of ADCs of the CSF in 11 (14%) patients because their subarachnoid spaces in the imaged area were less than 5 mm in the greatest minimal diameter.

There was a significant difference ($P < .001$) in the mean ADCs of the lesions among the four categories (Table 2). The mean ADC of malignant lymphomas, $(0.66 \pm 0.17) \times 10^{-3}$ mm^2/sec, was significantly smaller ($P < .001$) than that of carcinomas. That of carcinomas ($[1.13 \pm 0.43] \times 10^{-3}$ mm^2/sec) was significantly smaller ($P = .002$) than that of benign solid masses. That of benign solid masses ($[1.56 \pm 0.51] \times 10^{-3}$ mm^2/sec) was significantly smaller ($P = .035$) than that of benign cystic lesions ($[2.05 \pm 0.62] \times 10^{-3}$ mm^2/sec). No significant differences in the mean ADCs of the CSF and the spinal cord were seen among the four categories (Table 2). The mean ADCs of the CSF in 70 patients and of the spinal cord in all 81 patients were $(3.63 \pm 0.57) \times 10^{-3}$ mm^2/sec (exact 95% CI: 3.54×10^{-3}, 3.76×10^{-3}) and $(1.11 \pm 0.14) \times 10^{-3}$ mm^2/sec (exact 95% CI: 1.07×10^{-3}, 1.14×10^{-3}), respectively.

The mean ADC of SCCs with the conspicuous type of small foci necrosis ($n =$

6; [1.44 ± 0.41] × 10^{-3} mm^2/sec) was significantly larger ($P = .034$) than that of SCCs with the mild type of necrosis ($n = 12$; [1.03 ± 0.16] × 10^{-3} mm^2/sec).

The scatterplot of the ADCs of the four categories of the lesions is shown in Figure 1, and ROC curves for use of ADC values in distinguishing malignant from benign lesions and in distinguishing lymphomas from carcinomas are illustrated in Figure 2. The areas under the ROC curves for use of ADC values in differentiating malignant from benign lesions and in differentiating lymphomas from carcinomas were 0.87 ± 0.04 and 0.93 ± 0.04, respectively. When we used an ADC value of 1.22 × 10^{-3} mm^2/sec or less for predicting malignancy, the highest accuracy of 86% (70 of 81) was obtained, with 84% (41 of 49) sensitivity, 91% (29 of 32) specificity, 93% (41 of 44) positive predictive value, and 78% (29 of 37) negative predictive value (Table 3). ADC values of all malignant lymphomas and all but eight carcinomas were less than this threshold value. The eight exceptions were six SCCs (two metastatic SCCs in a lymph node, two SCCs of the nasal cavity, one SCC of the soft palate, and one SCC of the supraglottic larynx) and two adenocarcinomas of the thyroid. Among the six SCCs, pathologic analysis for small necrosis of SCCs was possible in five. All five SCCs showed the conspicuous type of small liquefactive necrosis, which was difficult to identify at MR imaging even in retrospect (Fig 3). In addition, two papillary adenocarcinomas of the thyroid showed a papillary-predominant growth pattern mixed with a follicular growth pattern that occupied 30%–40% of the tumors.

The ADCs in all benign cystic lesions (Fig 4) and in all but three benign solid lesions were larger than the threshold value. These three lesions included one reactive lymph node, one Warthin tumor in the parotid gland, and one parathyroid hyperplasia. Pathologic examination findings were available in two of these three lesions (one each of para-

TABLE 1
Diagnosis of 81 Lesions in the Head and Neck

Diagnosis of Lesions	No. of Lesions
Malignant lymphoma, non-Hodgkin lymphoma ($n = 13$)	
Low grade	2
Intermediate grade	8
High grade	3
Carcinoma ($n = 36$)	
SCC	22
Adenocarcinoma	14
Benign solid mass ($n = 22$)	
Pleomorphic adenoma	10
Warthin tumor	3
Parathyroid hyperplasia	2
Papilloma of the nasal cavity	1
Reactive lymph node	2
Hemangioma	2
Inflammation	2
Benign cystic lesion ($n = 10$)	
Branchial cleft cyst	6
Thyroglossal duct cyst	2
Inflammation in the retropharyngeal space	1
Warthin tumor	1
Total	81

TABLE 2
Mean ADCs of the Lesions, CSF, and Spinal Cord

Diagnosis	ADC of Lesions*†	ADC of CSF*‡	ADC of Spinal Cord*§
Malignant lymphoma ($n = 13$)	0.66 ± 0.17 (0.56, 0.76)	3.25 ± 0.94 (2.91, 3.59)	1.02 ± 0.15 (0.88, 1.16)
Carcinoma ($n = 36$)	1.13 ± 0.43 (0.99, 1.27)	3.74 ± 0.54 (3.61, 3.95)	1.13 ± 0.14 (1.07, 1.19)
Benign solid mass ($n = 22$)	1.56 ± 0.51 (1.34, 1.79)	3.70 ± 0.29 (3.57, 3.84)	1.13 ± 0.15 (1.04, 1.23)
Benign cystic lesion ($n = 10$)	2.05 ± 0.62 (1.63, 2.47)	3.59 ± 0.38 (3.19, 3.91)	1.07 ± 0.05 (1.02, 1.13)

Note.—Overall differences of the mean ADCs of the lesions, CSF, and the spinal cord in each category were calculated with the Kruskal-Wallis test. Data are the mean ± SD. Data in parentheses are the lower and upper limits of the 95% CI.

* ADC values are expressed as the (mean ± SD) × 10^{-3} mm^2/sec.

† $P < .001$.

‡ $P = .193$.

§ $P = .211$.

TABLE 3
Diagnostic Statistical Data for Use in Predicting Malignancy

Threshold of ADC Value (×10^{-3} mm^2/sec)	Sensitivity (%)	Specificity (%)	Accuracy (%)	Positive Predictive Value (%)	Negative Predictive Value (%)
≦0.65	14 (7/49)	100 (32/32)	48 (39/81)	100 (7/7)	43 (32/74)
≦1.01	53 (26/49)	91 (29/32)	68 (55/81)	90 (26/29)	56 (29/52)
≦1.22	84 (41/49)	91 (29/32)	86 (70/81)	93 (41/44)	78 (29/37)
≦1.56	96 (47/49)	59 (19/32)	81 (66/81)	78 (47/60)	90 (19/21)
≦2.75	100 (49/49)	3 (1/32)	62 (50/81)	61 (49/80)	100 (1/1)

Note.—Data in parentheses are the numbers of cases in patients that were used to calculate the percentages.

thyroid hyperplasia and Warthin tumor); the parathyroid hyperplasia consisted of densely proliferated chief cells with scant stroma, and the Warthin tumor showed papillary projection of the epithelial component with extensive lymphoid infiltration with germinal centers in the stroma (Fig 5).

When we limited analysis to malignant tumors, an ADC value of 0.84 × 10^{-3} mm^2/sec or less could be used to achieve the highest accuracy of 86% (42 of 49) for discriminating malignant lymphomas (Fig 6) from carcinomas, with 92% (12 of 13) sensitivity, 83% (30 of 36) specificity, 67% (12 of 18) positive predictive value, and 97% (30 of 31) negative predictive value (Table 4). The ADC in one high-grade malignant lymphoma exceeded the threshold value, and ADCs in six carcinomas were lower than this value. These six carcinomas included two SCCs in the tonsil, two SCCs in the hypopharynx, one metastatic SCC of the lymph nodes, and one papillary adenocarcinoma of the thyroid gland. Pathologically, the five SCC showed moderate (n = 1) or poor (n = 4) differentiation and had the mild type of small foci of liquefactive necrosis, and the papillary adenocarcinoma of the thyroid gland had a predominantly solid growth pattern and was associated with lymphocytic infiltration (sclerosing variant).

DISCUSSION

Diffusion of water protons in biologic tissues derives from the diffusion of extracellular water protons, transport of water protons through the cell membranes, and diffusion of intracellular water protons. The motion is disturbed by fibers, intracellular organelles, and macromolecules in the tissues. Since the water protons in each portion in the tissue contribute differently to the diffusion of the tissue (18), any architectural changes in the tissue, including the change in the proportion of extracellular to intracellular water protons, will alter the diffusion coefficient of the tissue. Thus, signal intensity of diffusion-weighted MR images and ADCs of the tissues vary according to the microstructure and physiologic state of the tissues.

It is no surprise that the mean ADC of the benign cystic lesions in this study was markedly higher than that of the other three categories of lesions, because the mobility of water protons is relatively freer in the fluid than it is in the other tissues. The differences in ADC values among cystic lesions may explain the varying protein concentration of the lesions (20). The higher protein component in the fluid will increase the viscosity and decrease the water proton mobility.

In this study, the mean ADC value of benign solid lesions was significantly higher than that of malignant tumors. The differences in ADCs may reflect distinct differences in the histopathologic features of the benign and malignant tumors. Generally, malignant tumors have enlarged nuclei, hyperchromatism, and angulation of nuclear contour, and they show hypercellularity (23). These histopathologic characteristics reduce the extracellular matrix and the diffusion space of water protons in the extracellular and intracellular dimensions, with a resultant decrease in the ADCs.

The mean ADC of carcinomas was significantly larger than that of malignant lymphomas. However, ADC values of several carcinomas were similar to those of lymphomas, and most of these ADC values were of poorly differentiated carcinomas. Malignant lymphomas and poorly differentiated carcinomas have much in common in histologic and cytologic features, and, therefore, supplementary special staining and immunohistochemical procedures are often required to discriminate between them. These tumors have more cellularity, larger and more angulated nuclei with more abundant macromolecular proteins, and less extracellular space than well or moderately differentiated carcinomas. Although there were some exceptions, such histopathologic changes may generally ex-

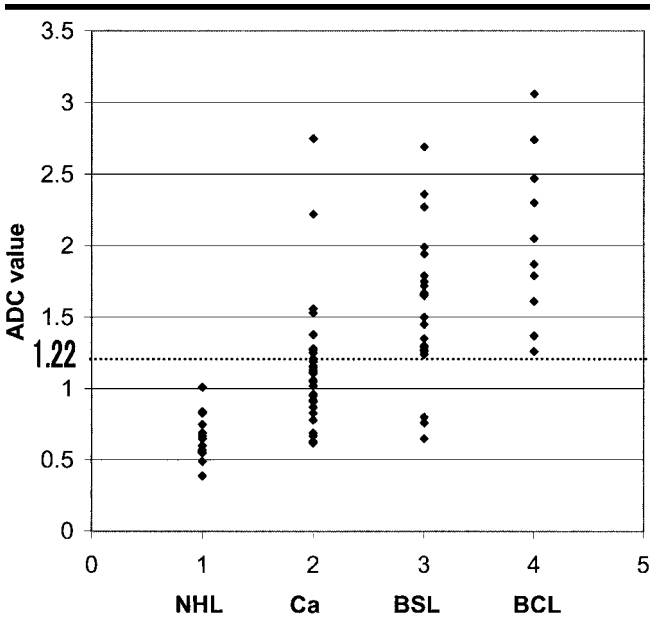

Figure 1. Scatterplot of the ADC values of 81 head and neck masses. When an ADC smaller than 1.22 × 10^{-3} mm^2/sec (dotted line) was used for differentiating benign from malignant lesions, the highest accuracy of 86% (70 of 81) was obtained. *NHL* = non-Hodgkin lymphoma lesions, *Ca* = carcinomas, *BSL* = benign solid lesions, *BCL* = benign cystic lesions.

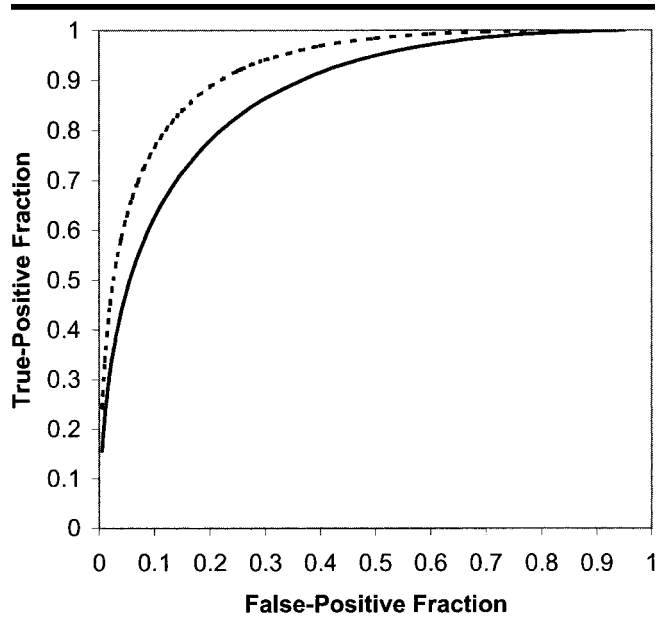

Figure 2. ROC curves of ADC values for use in differentiating malignancies from benign lesions (solid curve) and in differentiating lymphomas from carcinomas (dashed curve). The areas under the solid and dashed curves are 0.87 ± 0.04 and 0.92 ± 0.04, respectively.

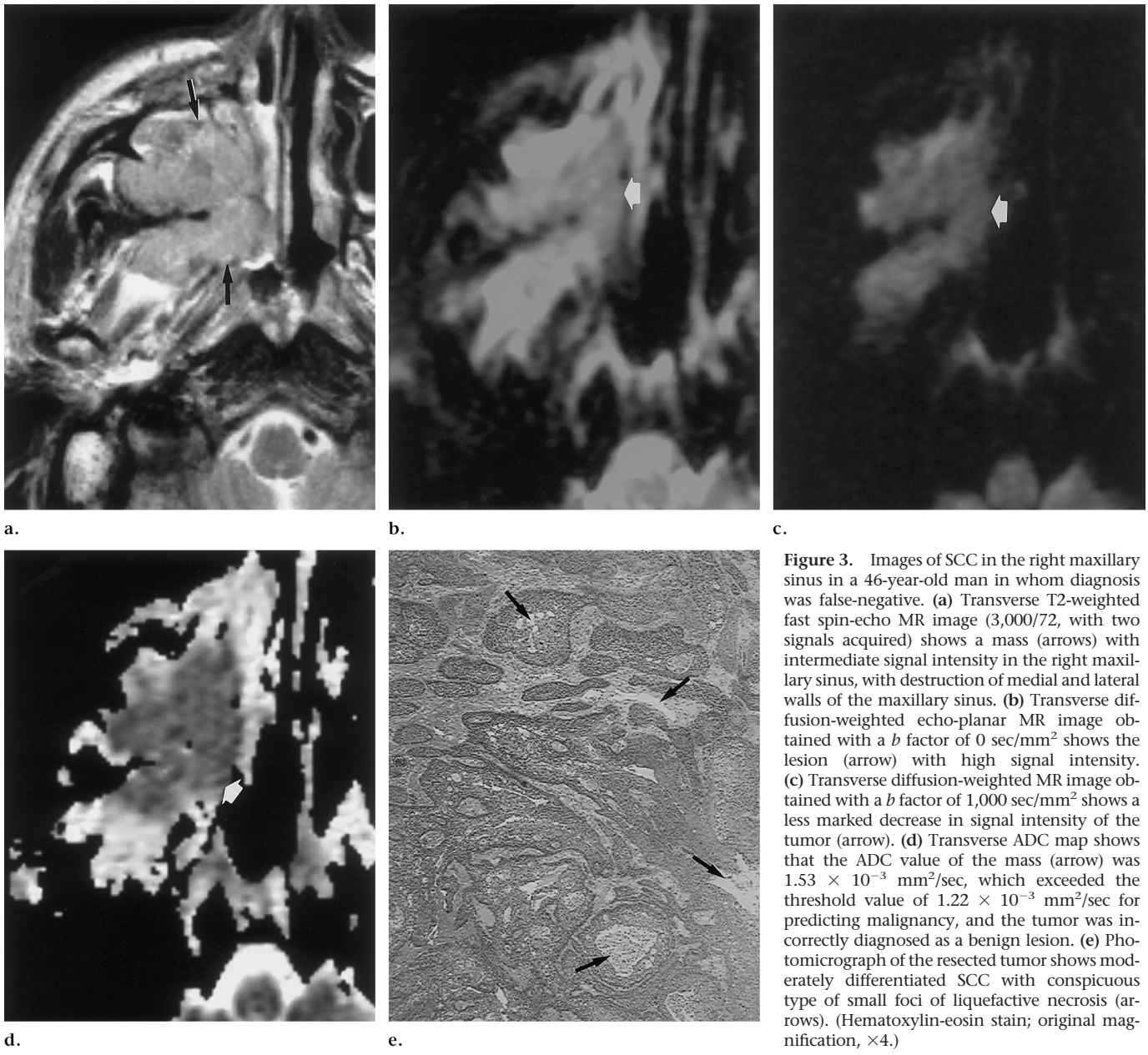

Figure 3. Images of SCC in the right maxillary sinus in a 46-year-old man in whom diagnosis was false-negative. **(a)** Transverse T2-weighted fast spin-echo MR image (3,000/72, with two signals acquired) shows a mass (arrows) with intermediate signal intensity in the right maxillary sinus, with destruction of medial and lateral walls of the maxillary sinus. **(b)** Transverse diffusion-weighted echo-planar MR image obtained with a *b* factor of 0 sec/mm^2 shows the lesion (arrow) with high signal intensity. **(c)** Transverse diffusion-weighted MR image obtained with a *b* factor of 1,000 sec/mm^2 shows a less marked decrease in signal intensity of the tumor (arrow). **(d)** Transverse ADC map shows that the ADC value of the mass (arrow) was 1.53×10^{-3} mm^2/sec, which exceeded the threshold value of 1.22×10^{-3} mm^2/sec for predicting malignancy, and the tumor was incorrectly diagnosed as a benign lesion. **(e)** Photomicrograph of the resected tumor shows moderately differentiated SCC with conspicuous type of small foci of liquefactive necrosis (arrows). (Hematoxylin-eosin stain; original magnification, ×4.)

TABLE 4
Diagnostic Statistical Data for Use in Discriminating Malignant Lymphoma from Carcinoma

Threshold of ADC Value ($\times 10^{-3}$ mm^2/sec)	Sensitivity (%)	Specificity (%)	Accuracy (%)	Positive Predictive Value (%)	Negative Predictive Value (%)
≦0.62	46 (6/13)	100 (36/36)	86 (42/49)	100 (6/6)	84 (36/43)
≦0.69	69 (9/13)	89 (32/36)	84 (41/49)	69 (9/13)	89 (32/36)
≦0.75	77 (10/13)	89 (32/36)	86 (42/49)	71 (10/14)	91 (32/35)
≦0.84	92 (12/13)	83 (30/36)	86 (42/49)	67 (12/18)	97 (30/31)
≦1.01	100 (13/13)	64 (23/36)	73 (36/49)	36 (13/36)	100 (23/23)

Note.—Data in parentheses are the numbers of cases in patients that were used to calculate the percentages.

plain the differences in ADCs among benign solid lesions, carcinomas, and malignant lymphomas.

Eight malignant tumors were falsely diagnosed as benign tumors on the basis of the ADC threshold value in this study. Of these tumors, six were primary SCC in the different organs or metastatic SCC in the lymph nodes, and the remaining two

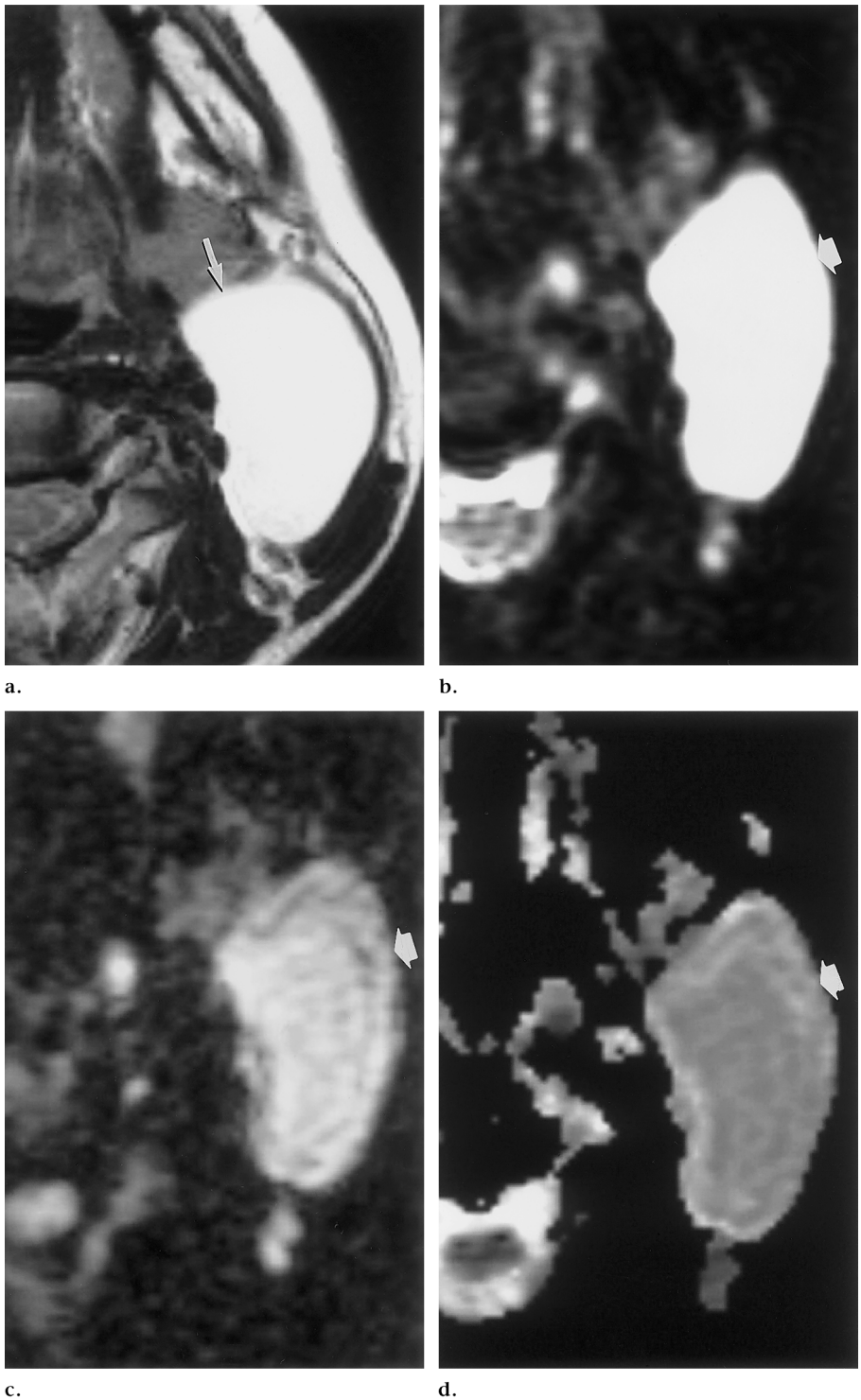

Figure 4. Images of a second branchial cleft cyst in a 30-year-old woman in whom the diagnosis was true-negative. **(a)** Transverse T2-weighted fast spin-echo MR image (3,000/72, with two signals acquired) shows a unilocular cyst (arrow) with high signal intensity in the left carotid space. **(b)** Transverse diffusion-weighted echo-planar MR image obtained with a *b* factor of 0 sec/mm^2 shows the lesion (arrow) with marked high signal intensity. **(c)** Transverse diffusion-weighted MR image obtained with a *b* factor of 1,000 sec/mm^2 shows that the signal intensity of the lesion (arrow) is markedly decreased. **(d)** Transverse ADC map shows that the ADC value of the cyst (arrow), which is 2.30×10^{-3} mm^2/sec, is high and that it is higher than the threshold value. The lesion was correctly diagnosed as a benign lesion.

were adenocarcinomas of the thyroid. Pathologic study findings revealed that five SCCs had the conspicuous type of small foci of liquefactive necrosis in the lesions that were difficult to identify at MR imaging even in retrospect. Pathologic specimens of the two papillary carcinomas of the thyroid contained considerable proportions of follicular component. ADC values of the necrotic portions of the tumors are high, as documented in the literature (20). Abundant extracellular fluid in the follicular portions may explain the high ADC value of carcinomas of the thyroid. Possible explanations for the high ADC values in the other malignant tumor (SCC) include micronecrosis in the tumors and ADC measurement in the hypervascular portions of the tumors that raised the proportion of the perfusion effect.

We inferred that the small foci of necrosis in the tumors, as confirmed by our pathologic study findings, that were not identifiable at MR imaging might be the major reasons for the high ADCs of malignant tumors in this study, because SCC and SCC metastasizing to the lymph node are likely to develop necrosis (21, 22). Although we selected macroscopic solid portions of the tumors for obtaining diffusion-weighted MR images and for measuring ADCs on the basis of MR findings in our series, we think it unavoidable to completely exclude the areas containing micronecrosis of the tumors in ADC measurement. MR imaging research (24) has revealed that the use of diffusion-weighted MR imaging was more reliable than that of other MR imaging techniques to identify micronecrosis of the tumors.

ADC values of three of 22 benign solid lesions were low and mimicked values of malignant tumors in this study. The disorders consisted of a reactive lymph node without macronecrosis, Warthin tumor, and parathyroid hyperplasia. In the reactive lymph node, a large amount of inflammatory cells often associated with lymphoid germinal centers and a varying amount of fibrosis in the stroma would disturb diffusion of the water protons in the extracellular fraction and lead to low ADCs. As confirmed by findings in the pathologic analyses, diffuse high cellularity of glandular cells with scant extracellular component may be the reason for the low ADCs of parathyroid hyperplasia. A proliferation of the epithelial component and intense lymphoid accumulation in the stroma may have limited the motion of the water

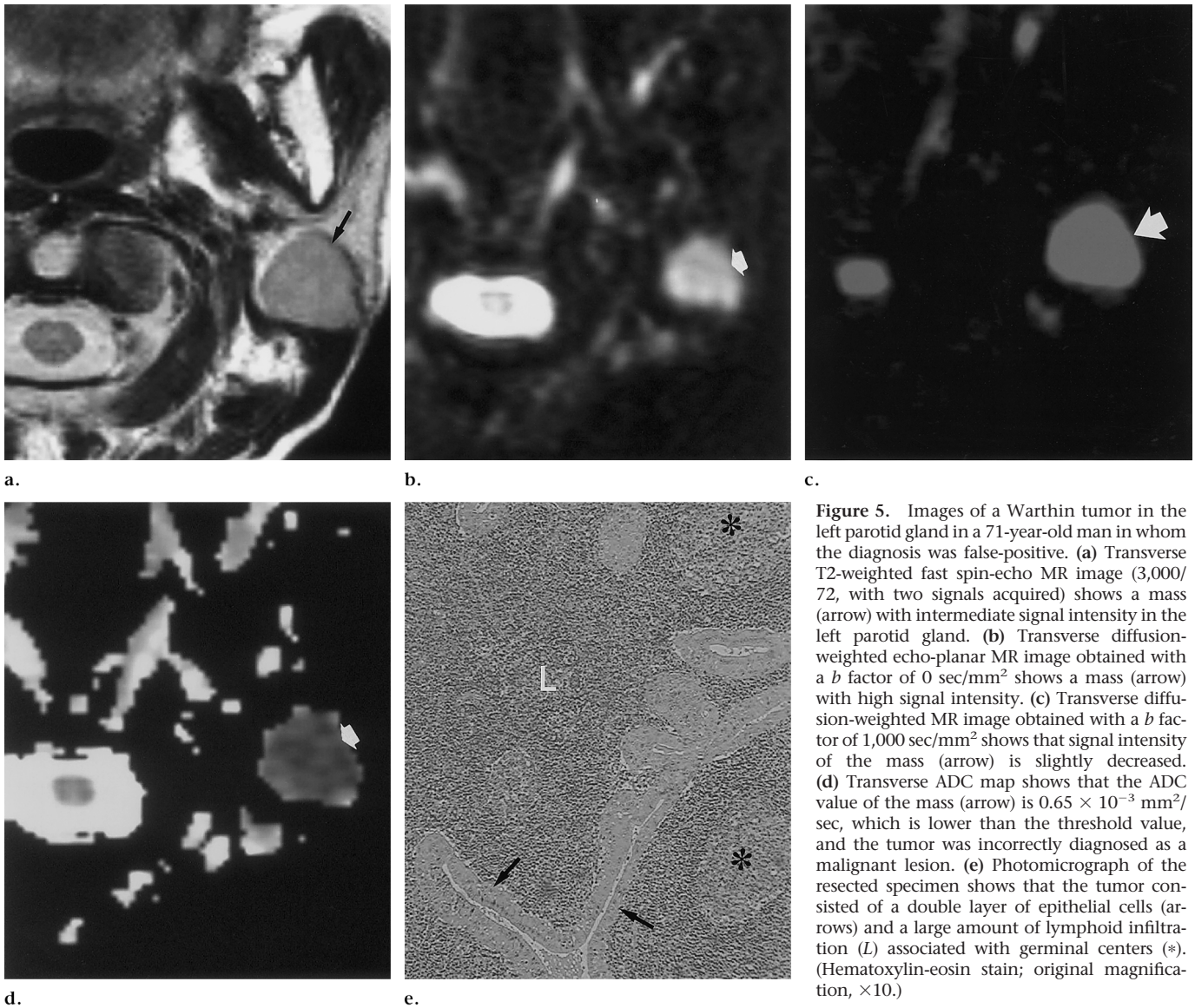

Figure 5. Images of a Warthin tumor in the left parotid gland in a 71-year-old man in whom the diagnosis was false-positive. **(a)** Transverse T2-weighted fast spin-echo MR image (3,000/72, with two signals acquired) shows a mass (arrow) with intermediate signal intensity in the left parotid gland. **(b)** Transverse diffusion-weighted echo-planar MR image obtained with a *b* factor of 0 sec/mm^2 shows a mass (arrow) with high signal intensity. **(c)** Transverse diffusion-weighted MR image obtained with a *b* factor of 1,000 sec/mm^2 shows that signal intensity of the mass (arrow) is slightly decreased. **(d)** Transverse ADC map shows that the ADC value of the mass (arrow) is 0.65×10^{-3} mm^2/sec, which is lower than the threshold value, and the tumor was incorrectly diagnosed as a malignant lesion. **(e)** Photomicrograph of the resected specimen shows that the tumor consisted of a double layer of epithelial cells (arrows) and a large amount of lymphoid infiltration (*L*) associated with germinal centers (*). (Hematoxylin-eosin stain; original magnification, ×10.)

protons in the extracellular space of the Warthin tumor.

The mean ADC value of CSF that was measured in the upper area of the neck in this study was in good agreement with that documented in a previous article (6). However, the measurement was precluded in 11 (14%) of our 81 patients because the subarachnoid space was too small. The ADCs of the spinal cord varied less than those of the CSF in the current study. Since the difference in area of the subarachnoid space would influence the velocity of the CSF and affect the ADC value, we believe the spinal cord should replace the CSF as a reference for head and neck lesions.

Although the echo-planar MR imaging sequence is likely to be associated with susceptibility artifacts, and therefore its use is limited because of these artifacts (25), a recent development (10,11,13) in echo-planar MR imaging technology enabled us to apply this MR technique even in the regions with high susceptibility artifacts. In this study, we further modified the echo-planar MR imaging sequence to improve the quality of images and to reduce the artifacts. We used a wider bandwidth and a thinner section to reduce distortion artifacts and chemical shift artifacts (26). Furthermore, we used a short echo time to shorten the imaging time and simultaneously obtained diffusion-weighted MR images with different *b* factors to avoid misregistration in acquiring ADCs. We also used a special antisusceptibility device that was put on the neck to improve the inhomogeneity of the magnetic field. Thus, the diffusion-weighted MR images were successfully obtained in most of our patients.

There were several limitations in our study. First, although we used the improved sequence to reduce the susceptibility artifacts, image distortions along the phase-encoding direction were unavoidable to some degree, and, therefore, the ADC values measured in small lesions might be inaccurate. Second, we were unable to measure ADC values of the lesions located adjacent to the air-containing organs because of susceptibility artifacts. Third, the number of cases and the correlation of ADCs of lesions with his-

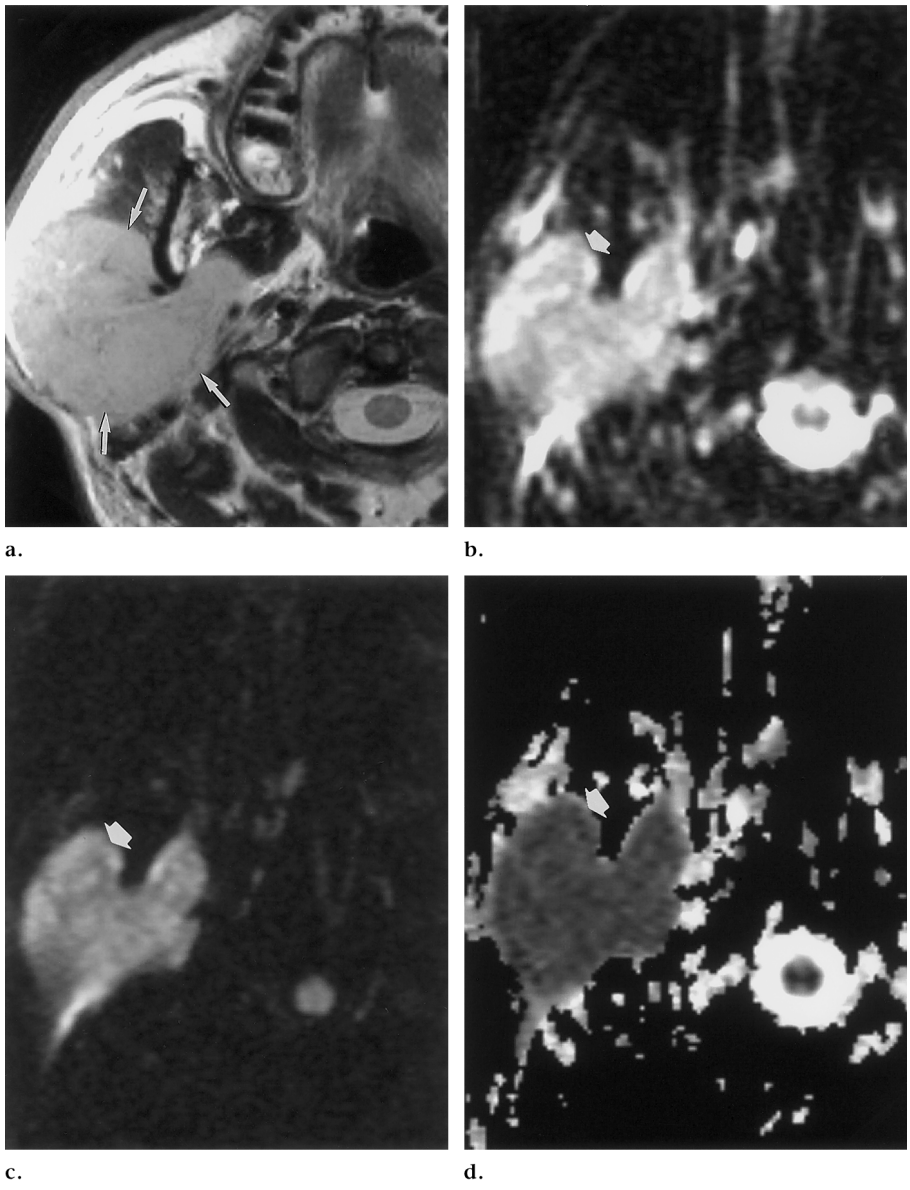

Figure 6. Images of non-Hodgkin lymphoma (diffuse large B cell, intermediate grade) in the right parotid gland in a 37-year-old man in whom the diagnosis was true-positive. **(a)** Transverse T2-weighted fast spin-echo MR image (3,000/72, with two signals acquired) shows a homogeneous mass (arrows) with intermediate signal intensity in the right parotid gland. **(b)** Transverse diffusion-weighted echo-planar MR image obtained with a *b* factor of 0 sec/mm^2 shows the mass (arrow) with high signal intensity. **(c)** Transverse diffusion-weighted MR image obtained with a *b* factor of 1,000 sec/mm^2 shows a slight decrease in signal intensity of the mass (arrow). **(d)** Transverse ADC map shows that the ADC value of the mass (arrow) is 0.67×10^{-3} mm^2/sec, which is lower than the threshold value, and the lesion was correctly diagnosed as a malignant lesion.

topathologic findings were limited. We think a further investigation in a larger series is necessary to clarify the correlation between the ADC values and histopathologic findings. Finally, the threshold value for predicting malignancy or for differentiating lymphomas from carcinomas should be determined for each MR imaging system, since there are some variations in MR units, pulse sequences, and operation of the units. In the future, this kind of a study should be performed in a larger number of cases to verify the results of our preliminary study, and the results of diffusion-weighted MR imaging should be compared with those of clinical MR examination for diagnosis and staging of cancers in the head and neck region.

In conclusion, diffusion-weighted MR imaging may be used to help in the characterization of head and neck lesions, and its findings may provide useful supplementary information before surgery or biopsy.

Acknowledgments: We thank Hitoshi Ueda and Tadashi Miyasaka, Department of Radiology, Shinshu University, Nagano, Japan, for providing helpful technical support and for performing many of the tasks associated with this project. The contribution of Honggang Liu, PhD, MD, Second Department of Pathology, Shinshu University, Nagano, Japan, to our research is greatly appreciated.

References

1. Le Bihan D, Breton E, Lallemand D, Grenier P, Cabanis E, Laval-Jeantet M. MR imaging of intravoxel incoherent motions: application to diffusion and perfusion in neurologic disorders. Radiology 1986; 161:401–407.
2. Moseley ME, Kucharczyk J, Mintorovitch J, et al. Diffusion-weighted MR imaging of acute stroke: correlation with T2-weighted and magnetic susceptibility-enhanced MR imaging in cats. AJNR Am J Neuroradiol 1990; 11:423–429.
3. Warach S, Gaa J, Siewart B, et al. Acute human stroke studied by whole brain echo planar diffusion-weighted magnetic resonance imaging. Ann Neurol 1995; 37: 231–241.
4. Sorensen AG, Buananno FS, Gonzalez RG, et al. Hyperacute stroke: evaluation with combined multisection diffusion-weighted and hemodynamically weighted echo-planar imaging. Radiology 1996; 199:391–401.
5. Sakuma H, Nomura Y, Takeda K, et al. Adult and neonatal brain: diffusion anisotropy and myelination with diffusion-weighted MR imaging. Radiology 1991; 180:229–233.
6. Tanner SF, Ramenghi LA, Ridgway JP, et al. Quantitative comparison of intrabrain diffusion in adults and preterm and term neonates and infants. AJR Am J Roentgenol 2000; 174:1643–1649.
7. LeBihan D, Douek P, Argyropoulou M, Turner R, Patronas N, Fulham M. Diffusion and perfusion magnetic resonance imaging in brain tumors. Top Magn Reson Imaging 1993; 5:25–31.
8. Maeda M, Kawamura Y, Tamagawa Y, et al. Intravoxel incoherent motion (IVIM) MRI in intracranial, extraaxial tumors and cysts. J Comput Assist Tomogr 1992; 16:514–518.
9. Tien RD, Felsberg GJ, Friedman H, Brown M, MacFall J. MR imaging of high-grade cerebral gliomas: value of diffusion-weighted echoplanar pulse sequences. AJR Am J Roentgenol 1994; 162:671–677.
10. Namimoto T, Yamashita Y, Sumi S, Tang Y, Takahashi M. Focal liver masses: characterization with diffusion-weighted echo-planar MR imaging. Radiology 1997; 204: 739–744.
11. Kim T, Murakami T, Takahashi S, Hori M, Tsuda K, Nakamura H. Diffusion-weighted single-shot echoplanar MR imaging for liver disease. AJR Am J Roentgenol 1999; 173:393–398.
12. Baur A, Stäbler A, Brüning R, et al. Diffusion-weighted MR imaging of bone marrow: differentiation of benign versus pathologic compression fractures. Radiology 1998; 207:349–356.
13. Yamashita Y, Namimoto T, Mitsuzaki K,

et al. Mucin-producing tumor of the pancreas: diagnostic value of diffusion-weighted echo-planar MR imaging. Radiology 1998; 208:605–609.
14. Moteki T, Ishizaka H. Evaluation of cystic ovarian lesions using apparent diffusion coefficient calculated from reordered turboflash MR images. Magn Reson Imaging 1999; 17:955–963.
15. Baker LL, Dillon WP, Hieshima GB, Dowd CF, Frieden IJ. Hemangiomas and vascular malformations of the head and neck: MR characterization. AJNR Am J Neuroradiol 1993; 14:307–314.
16. Thomsen C, Henriksen O, Ring P. In vivo measurement of water self diffusion in the human brain by magnetic resonance imaging. Acta Radiol 1987; 28:353–361.
17. Le Bihan D. Molecular diffusion nuclear magnetic resonance. Magn Reson Q 1991; 7:1–30.
18. National Cancer Institute sponsored study of classifications of non-Hodgkin's lymphomas: summary and description of a working formulation for clinical usage—the non-Hodgkin's lymphoma pathologic classification project. Cancer 1982; 49: 2112–2135.
19. Szafer A, Zhong J, Gore JC. Theoretical model for water diffusion in tissues. Magn Reson Med 1995; 33:687–712.
20. Kim YJ, Chang KY, Song IC, et al. Brain abscess and necrotic or cystic brain tumor: discrimination with signal intensity on diffusion weighted MR imaging. AJR Am J Roentgenol 1998; 171:1487–1490.
21. Yousem DM, Montone KT. Head and neck lesions: radiologic-pathologic correlations. Radiol Clin North Am 1998; 36: 983–1014.
22. van den Brekel MW, Stel HV, Castelijns JA, et al. Cervical lymph node metastasis: assessment of radiologic criteria. Radiology 1990; 177:379–384.
23. Anderson JR. Tumours. I. General features, types and examples. In: Anderson JR, ed. Muir's textbook of pathology. 20th ed. London, England: Edward Arnold, 1985; 12.1–12.49.
24. Lang P, Wendland MF, Saeed M, et al. Osteogenic sarcoma: noninvasive in vivo assessment of tumor necrosis with diffusion-weighted MR imaging. Radiology 1998; 206:227–235.
25. Le Bihan D, Turner R, Douek P, Patronas N. Diffusion MR imaging: clinical application. AJR Am J Roentgenol 1992; 159: 591–599.
26. Edelman RR, Wielopolski P, Schmitt F. Echo-planar MR imaging. Radiology 1994; 192:600–612.